

Near-field heat transfer between multilayer hyperbolic metamaterials

Svend-Age Biehs¹, Philippe Ben-Abdallah^{2,3}

¹ *Institut für Physik, Carl von Ossietzky Universität, D-26111 Oldenburg, Germany.*

² *Laboratoire Charles Fabry, UMR 8501, Institut d'Optique, CNRS,*

Université Paris-Sud 11, 2, Avenue Augustin Fresnel, 91127 Palaiseau Cedex, France and

³ *Université de Sherbrooke, Department of Mechanical Engineering, Sherbrooke, PQ J1K 2R1, Canada.**

(Dated: September 23, 2018)

We review the near-field radiative heat flux between hyperbolic materials focusing on multilayer hyperbolic meta-materials. We discuss the formation of the hyperbolic bands, the impact of ordering of the multilayer slabs, as well as the impact of the first single layer on the heat transfer. Furthermore, we compare the contribution of surface modes to that of hyperbolic modes. Finally, we also compare the exact results with predictions from effective medium theory.

PACS numbers:

I. INTRODUCTION

Hyperbolic materials (HM) [1, 2] have attracted a lot of attention in the last years due to their unique properties. It could be shown that they allow for a broadband enhanced LDOS [3], broadband enhanced spontaneous emission [4–15], hyperbolic lensing [16–20], negative refraction [21, 22], super absorption [23], enhanced Förster energy transfer [24–26], and self-induced torques [27]. HM can be artificially fabricated by a periodic layout of sub-wavelength metal and dielectric components for applications in the visible. On the other hand, for applications in the infrared it is more beneficial to combine phonon-polaritonic/semi-conductor and dielectric components [22, 28–30, 32, 33]. Besides such hyperbolic meta-material (HMM) structures there exist also quite a number of natural HM [34–38] for applications in the visible and infrared.

Here, we are mainly interested in the application of HM in the context of thermal radiation in the near-field regime [39–43]. It is well known that in this distance regime the radiative heat flux can be much larger than that of a blackbody due to the extra-contribution of evanescent waves such as surface phonon polaritons [39–43], for instance. This super-Planckian effect has been measured by many different experiments using different geometries and materials [44–56], in the last ten years. So far, there is only one experiment which has measured the heat flux of a HM [33], although HM seem to have quite interesting features for near-field thermal radiation. For example, it was shown that HM could serve as an analogue of a blackbody for near-field thermal radiation [28], allowing for broadband thermal radiation [28, 29]. Furthermore, it has been shown that HM can be used for near-field thermophotovoltaic applications [57, 58], that HM have a large penetration depth of thermal radiation [59, 60] which is an advantage also for the transport of near-field thermal radiation over far-

field distances [61]. Also the possibility of having larger conduction by thermal radiation inside a HM than conduction by phonons and electrons has been discussed [62] as well as the thermodynamical potentials, the general laws of thermal radiation inside HM [63] and the coherence properties in the vicinity of HM [64]. Recently, also tunable hyperbolic thermal emitters have been introduced [65] and it was proposed to make use of the hyperbolic 2D plasmons in graphene ribbons for elevated near-field heat fluxes [66].

In this article we review the near-field radiative heat flux between HM by focusing on multilayer hyperbolic meta-materials (mHMM), because these structures can easily be fabricated and the numerical exact treatment is relatively simple in this case. Many researchers have already studied the radiative heat flux of layered materials in different contexts. For example, the impact of dissipation of thin layers was discussed [67] as well as the impact of surface-polariton coupling inside thin metal [68] and later also dielectric [69, 70] coatings. Real multilayer structures were discussed in the context of heat radiation between two photonic crystals [71, 72] and inside of photonic crystals [72–74]. The contribution of surface Bloch modes was quantified [75, 76] and the S-matrix and impedance method were introduced for near-field heat transfer calculations [77, 78]. In the following we will in particular make use of the S-matrix method.

The outline of our work is as follows: first, we will introduce the concept of HM as well as the basic expressions needed to calculate the radiative heat flux for such materials in Sec. II and III. In Sec. IV we will discuss in detail the near-field heat transfer between mHMM. Finally in Sec. V we summarize the main results and give some outlook to future work on this topic.

II. HYPERBOLIC MEDIA

HM are a special class of anisotropic uni-axial media. In such anisotropic uni-axial media the permittivity tensor with respect to the principal axis can be written as a

*Electronic address: s.age.biehs@uni-oldenburg.de, pba@institutoptique.fr

diagonal matrix of the form [79]

$$\underline{\underline{\epsilon}} = \begin{pmatrix} \epsilon_{\perp} & 0 & 0 \\ 0 & \epsilon_{\perp} & 0 \\ 0 & 0 & \epsilon_{\parallel} \end{pmatrix}. \quad (1)$$

The permittivity ϵ_{\parallel} is the permittivity 'seen' by an electric field which is parallel to optical axis which coincides here with the z-axis, whereas the permittivity ϵ_{\perp} is the permittivity 'seen' by an electric field which is perpendicular to the optical axis. For the sake of clarity let us in this section neglect dissipation, i.e. we assume that the permittivities are purely real numbers. Then one can easily classify different types of media [1, 2]:

1. If $\epsilon_{\perp} > 0$ and $\epsilon_{\parallel} > 0$ then the medium is dielectric. For $\epsilon_{\perp} \neq \epsilon_{\parallel}$ the medium is uni-axial and for $\epsilon_{\perp} = \epsilon_{\parallel}$ it is isotropic.
2. If $\epsilon_{\perp} < 0$ and $\epsilon_{\parallel} < 0$ then the medium is metallic. Again, for $\epsilon_{\perp} \neq \epsilon_{\parallel}$ the medium is uni-axial and for $\epsilon_{\perp} = \epsilon_{\parallel}$ it is isotropic.
3. If $\epsilon_{\perp} > 0$ and $\epsilon_{\parallel} < 0$ then the medium is called a type I hyperbolic material.
4. If $\epsilon_{\perp} < 0$ and $\epsilon_{\parallel} > 0$ then the medium is called a type II hyperbolic material.

That means that we can define HM by the property $\epsilon_{\perp}\epsilon_{\parallel} < 0$. An extension towards uni-axial magnetic materials with hyperbolic properties is straightforward [1, 2].

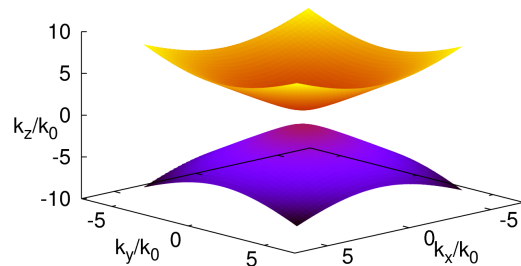
In order to see the difference in the optical properties of the different classes of uni-axial materials, one can solve for the eigensolutions of the vector-wave equation of the electromagnetic fields which will give the dispersion relations of the two linear independent eigenmodes, the so-called ordinary and extra-ordinary modes. The dispersion relation of the ordinary modes is given by [79]

$$\frac{k_x^2 + k_y^2 + k_z^2}{\epsilon_{\perp}} - \frac{\omega^2}{c^2} = 0 \quad (2)$$

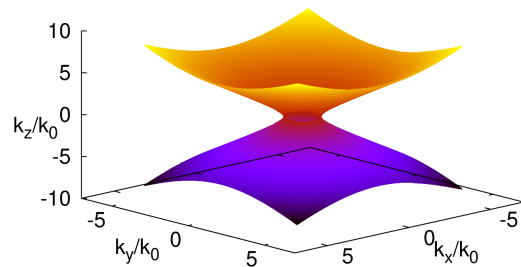
and the dispersion relation of the extra-ordinary modes is given by [79]

$$\frac{k_x^2 + k_y^2}{\epsilon_{\parallel}} + \frac{k_z^2}{\epsilon_{\perp}} - \frac{\omega^2}{c^2} = 0. \quad (3)$$

From these relations it is obvious that only the extra-ordinary modes are subjected to the anisotropy, since both permittivities ϵ_{\perp} and ϵ_{\parallel} enter in their dispersion relation. As a consequence only for these modes the difference between dielectric and hyperbolic modes can be seen. This difference can be made obvious when fixing the frequency and plotting the dispersion relations in k-space. These iso-frequency curves are for dielectrics ellipsoids. On the other hand, for a type I (type II) hyperbolic material these iso-frequency curves are two-sheeted (one-sheeted) hyperboloids as sketched in Fig. 1. From these iso-frequency curves the main feature of HM becomes



(a) type I



(b) type II

Figure 1: Plot of the isofrequency curves for the extraordinary modes in k-space for a (a) type I hyperbolic material with $\epsilon_{\parallel} = -0.7$ and $\epsilon_{\perp} = 1$ and a (b) type II hyperbolic material with $\epsilon_{\parallel} = 0.7$ and $\epsilon_{\perp} = -1$.

apparent: In principle, HM allow for propagating wave solutions with arbitrarily large wave numbers, whereas for dielectric media the wave-vectors are bounded by $\max(\sqrt{\epsilon_{\parallel}}k_0, \sqrt{\epsilon_{\perp}}k_0)$ where $k_0 = \omega/c$ is the modulus of the wave-vector in vacuum. Of course, in practice also the allowed wave-vectors inside HM are limited by the properties of the material's crystalline structure [80, 81], but they are generally speaking larger than in dielectric uni-axial media. Note that there are no propagating wave solutions for the metallic case because $\epsilon_{\perp} < 0$ and $\epsilon_{\parallel} < 0$. Since $\epsilon_{\perp} < 0$ for the type II HM, there are also no ordinary-mode solutions for type II HM.

One might think that materials fulfilling the condition $\epsilon_{\perp}\epsilon_{\parallel} < 0$ are rare to find, but in fact this is not true. There are many different natural bulk HM such as hexagonal boron nitride, tetradymites, etc. which have hyperbolic bands in the visible, near-infrared or infrared regime. For an overview of different natural HM listing the different respective hyperbolic bands we refer the reader to the references [34–38]. Apart from natural HM there also exists the possibility to artificially fabricate hyperbolic

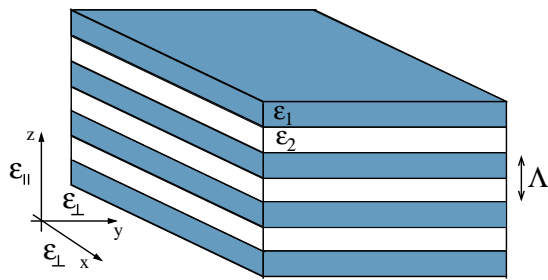


Figure 2: Sketch of a hyperbolic multilayered periodic structure with a period Λ composed of materials with permittivities ϵ_1 and ϵ_2 .

meta-materials using nanostructuring methods. Such hyperbolic meta-materials can be multilayer structures consisting of alternating layers of dielectric and metallic slabs (mHMM) or of periodic metallic nanorod structures which are immersed in a dielectric host (wHMM) with a subwavelength periodicity, for instance. The advantage of such artificial structures is that the broadness and spectral position of the hyperbolic bands can be tailored to some extent by choosing different materials and different filling fractions of the combined materials.

In order to have a simple model for the permittivities of hyperbolic meta-materials one can use the well-known expressions of effective medium theory (EMT). For example the effective permittivities of mHMM as sketched in Fig. 2 can be modelled in the long-wavelength regime by [79]

$$\epsilon_{\perp} = f\epsilon_1 + (1-f)\epsilon_2, \quad (4)$$

$$\epsilon_{\parallel} = \left(\frac{f}{\epsilon_1} + \frac{1-f}{\epsilon_2} \right)^{-1}, \quad (5)$$

where f is the volume filling fraction of material 1 with permittivity ϵ_1 and $1-f$ is the volume filling fraction of material 2 with permittivity ϵ_2 . These expressions, which can be obtained by an averaging of the electric field over one period of the structure, are strictly speaking only meaningful when the periodicity Λ of the meta-material structure is much smaller than the wavelength but even for Λ much smaller than the wavelength the EMT results can lead to wrong predictions [11–15, 30, 82] so that some care needs to be exercised when using these EMT expressions. Nonetheless, they are quite helpful for determining the hyperbolic frequency bands of a meta-material structure in a simple way.

As an example, we show in Fig. 3 a plot of the real parts of the effective permittivities of a SiC/Ge mHMM structure with $\epsilon_1 = \epsilon_{\text{SiC}}$ and $\epsilon_2 = \epsilon_{\text{Ge}} = 16$, where [83]

$$\epsilon_{\text{SiC}}(\omega) = \epsilon_{\infty} \frac{\omega^2 - \omega_{\text{LO}}^2 + i\gamma\omega}{\omega^2 - \omega_{\text{TO}}^2 + i\gamma\omega}, \quad (6)$$

with $\epsilon_{\infty} = 6.7$, $\omega_{\text{TO}} = 1.495 \cdot 10^{14}$ rad/s, $\omega_{\text{LO}} = 1.827 \cdot 10^{14}$ rad/s and $\gamma = 0.9 \cdot 10^{12}$ rad/s. It can be seen that by changing the filling fraction f for SiC the broadness of

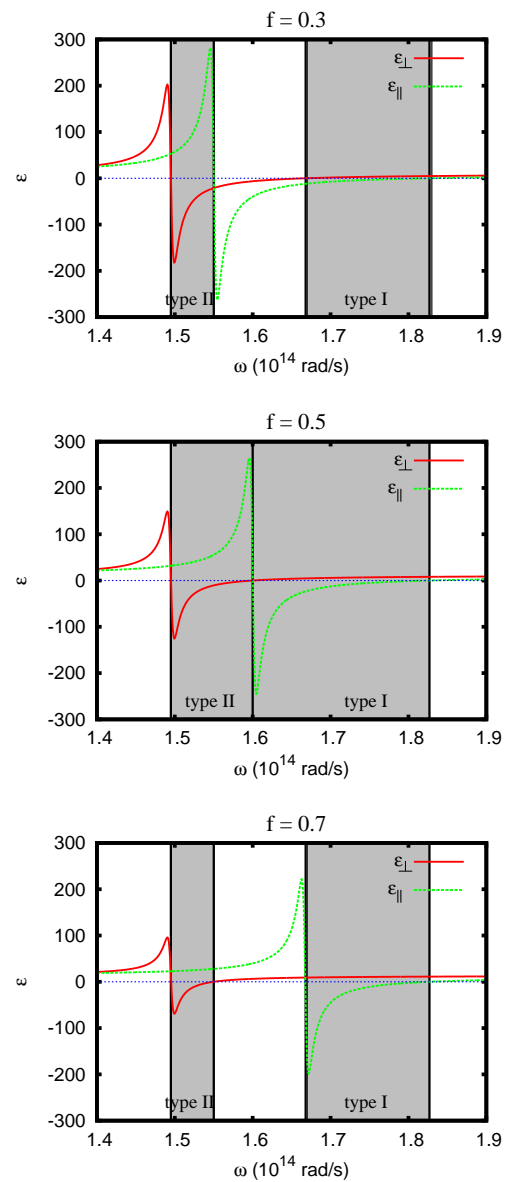


Figure 3: Plot of the real parts of the permittivities ϵ_{\parallel} and ϵ_{\perp} for a SiC/Ge mHMM using the EMT expressions from Eqs. (4) and (5) for filling fractions $f = 0.3, 0.5, 0.7$ of SiC. The hyperbolic frequency bands of type I and II (in grey) lie in the reststrahlen band $\omega_{\text{TO}} < \omega < \omega_{\text{LO}}$ of SiC where $\omega_{\text{TO}} = 1.495 \times 10^{14}$ rad/s and $\omega_{\text{LO}} = 1.827 \times 10^{14}$ rad/s are the frequencies of the transversal and longitudinal phonons in SiC.

the hyperbolic bands can be controlled where the largest hyperbolic bands are obtained for $f = 0.5$. In this case both hyperbolic bands are extended over the whole reststrahlen band of SiC [84] in which SiC has metal-like properties, i.e. its permittivity is negative. Of course, the overall hyperbolic frequency band can be made larger by using materials with a broader reststrahlen band or by using two phonon-polaritonic materials like SiC and GaN with adjacent reststrahlen bands. Note that al-

though metals would have a negative permittivity over the whole frequency range below the plasma frequency of the metal, they are less advantageous than phonon-polaritonic materials mHMM structures in the infrared, because the losses become quite large for thin metallic slabs [85].

III. HEAT FLUX FORMULA FOR ANISOTROPIC MEDIA

In order to determine the heat flux between two HM at temperatures T_1 and T_2 which are separated by vacuum gap of thickness d as sketched in Fig. 4 the heat flux expression of Polder and van Hove [86] which is based on Rytov's fluctuational electrodynamics has been generalized to anisotropic media [87–90]. The resulting heat flux expression can be written as

$$\Phi = \int_0^\infty \frac{d\omega}{2\pi} [\Theta(\omega, T_1) - \Theta(\omega, T_2)] \Phi_\omega. \quad (7)$$

where ($i = 1, 2$)

$$\Theta(\omega, T_i) = \frac{\hbar\omega}{e^{\frac{\hbar\omega}{k_B T_i}} - 1}, \quad (8)$$

is the thermal part of the mean energy of a quantum mechanical harmonic oscillator at temperature T_i ; $2\pi\hbar$ is Planck's constant and k_B is Boltzmann's constant. For the reduced spectral heat flux we obtain

$$\Phi_\omega = \int \frac{d^2\kappa}{(2\pi)^2} \mathcal{T}(\omega, \kappa; d) \quad (9)$$

introducing the transmission coefficient

$$\mathcal{T}(\omega, \kappa; d) = \begin{cases} \text{Tr}[(\mathbb{1} - \mathbf{R}_2^\dagger \mathbf{R}_2) \mathbf{D}^{12} (\mathbb{1} - \mathbf{R}_1 \mathbf{R}_1^\dagger) \mathbf{D}^{12\dagger}], & \kappa < k_0 \\ \text{Tr}[(\mathbf{R}_2^\dagger - \mathbf{R}_2) \mathbf{D}^{12} (\mathbf{R}_1 - \mathbf{R}_1^\dagger) \mathbf{D}^{12\dagger}] e^{-2|\gamma_0|d}, & \kappa > k_0 \end{cases} \quad (10)$$

which has the property $\mathcal{T} \in [0, 2]$ which is due to the fact, that the so defined transmission coefficients accounts for both polarizations as well as for possible depolarization effects. The 2x2 reflection matrix of the two interfaces are given by ($i = 1, 2$)

$$\mathbf{R}_i = \begin{pmatrix} r_i^{ss}(\omega, \kappa) & r_i^{sp}(\omega, \kappa) \\ r_i^{ps}(\omega, \kappa) & r_i^{pp}(\omega, \kappa) \end{pmatrix}. \quad (11)$$

The Fresnel reflection coefficients $r_i^{ss}(\omega, \kappa)$, $r_i^{ps}(\omega, \kappa)$ etc. are the usual reflection coefficients of interface i describing the scattering of an incoming s-polarized plane wave into a s-polarized or p-polarized wave etc. The Fabry-Pérot-like 'denominator' is defined as

$$\mathbf{D}^{12} = (\mathbb{1} - \mathbf{R}_1 \mathbf{R}_2 e^{2i\gamma_0 d})^{-1}. \quad (12)$$

Here $\gamma_0 = \sqrt{\kappa^2 - k_0^2}$ is the wave-vector component normal to the interfaces of the two anisotropic materials

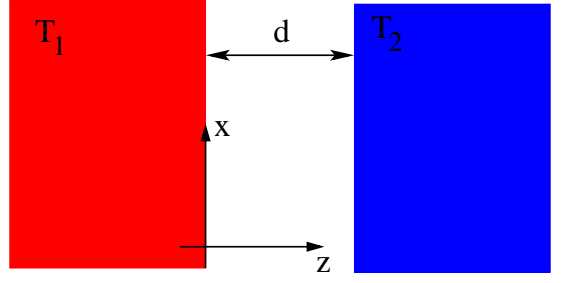


Figure 4: Sketch of two semi-infinite materials at two different temperatures T_1 and T_2 which are separated by a vacuum gap of thickness d .

and $\kappa = (k_x, k_y)^t$ is the wave-vector component parallel to the interfaces (see Fig. 4). For more details on the derivation and definition of the different quantities we refer the reader to Ref. [87], for instance. From the above expressions it becomes clear that the transmission coefficient \mathcal{T} takes into account the propagating wave contributions ($\kappa < k_0$) as well as the evanescent wave contributions ($\kappa > k_0$). The evanescent wave contribution is the reason for having super-Planckian heat transfer at the nanoscale [86]. On the other hand, for the propagating wave contribution the blackbody limit cannot be overcome as has been proved once more for anisotropic media in the framework of fluctuational electrodynamics in Ref. [91], recently.

Finally, in the special case where we consider two uniaxial materials having an optical axis which is normal to the interface the above expressions simplify, because in this case the reflection matrix becomes diagonal, i.e. we have $r_i^{sp} = r_i^{ps} = 0$, with the diagonal components

$$r_i^{ss} = \frac{\gamma_0 - \gamma_{i,s}}{\gamma_0 + \gamma_{i,s}} \equiv r_i^s(\omega, \kappa), \quad (13)$$

$$r_i^{pp} = \frac{\epsilon_{i,\parallel} \gamma_0 - \gamma_{i,p}}{\epsilon_{i,\parallel} \gamma_0 + \gamma_{i,p}} \equiv r_i^p(\omega, \kappa). \quad (14)$$

Furthermore, when the optical axis coincides with the surface normal the ordinary (extra-ordinary) modes coincide with the s-polarized (p-polarized) modes. Hence, the z-components of the wave-vector for s- and p-polarization $\gamma_{i,s/p}$ are determined by the dispersion relations in Eqs. (2) and (3) yielding

$$\gamma_{i,s} = \sqrt{\epsilon_{i,\perp} k_0^2 - \kappa^2}, \quad (15)$$

$$\gamma_{i,p} = \sqrt{\epsilon_{i,\perp} k_0^2 - \frac{\epsilon_{i,\perp}}{\epsilon_{i,\parallel}} \kappa^2}. \quad (16)$$

Then the transmission coefficient simplifies to $\mathcal{T} = \mathcal{T}_s + \mathcal{T}_p$ where the transmission coefficients for the two polarization states of light are given by ($\lambda = s, p$)

$$\mathcal{T}_\lambda(\omega, \kappa; d) = \begin{cases} \frac{(1 - |r_1^\lambda|^2)(1 - |r_2^\lambda|^2)}{|1 - r_1^\lambda r_2^\lambda \exp(2i\gamma_0 d)|^2}, & \kappa < k_0 \\ 4 \frac{\text{Im}(r_1^\lambda) \text{Im}(r_2^\lambda) e^{-2|\gamma_0|d}}{|1 - r_1^\lambda r_2^\lambda \exp(2i\gamma_0 d)|^2}, & \kappa > k_0 \end{cases} \quad (17)$$

with $\mathcal{T}_\lambda \in [0, 1]$. By setting $\epsilon_{i,\perp} = \epsilon_{i,\parallel} \equiv \epsilon_i$ we retrieve the well-known results of Polder-van Hove [86] describing the heat flux between two isotropic semi-infinite materials with permittivities ϵ_i . The same expressions can of course also be used for magneto-optical uni-axial materials by adding the magnetic properties to the reflection coefficients [93, 94].

IV. MULTILAYER HMM

A. Formation of hyperbolic bands

First, let us see how the hyperbolic bands are formed in mHMM. To this end, we first chose a SiC/Ge mHMM with a filling fraction of $f = 0.5$, because in this case the hyperbolic bands are the broadest as shown in Fig. 3. Furthermore, we choose 10 nm for the germanium and the SiC layers so that $\Lambda = 20$ nm and we chose a vacuum gap of $d = 10$ nm. In order to show the formation of the hyperbolic bands we plot the transmission coefficient for p-polarized light in Eq. (17) for two SiC bulk materials first in Fig. 5(a). For SiC we choose $\epsilon_{\parallel} = \epsilon_{\perp} = \epsilon_{\text{SiC}}$. Then we add successively 10 nm layers of Ge such that we obtain a mHMM with $N = 9$ SiC/Ge unit cells and $f = 0.5$. The reflection coefficients r_i^s and r_i^p for these structures are calculated by the S-matrix method [103] and then used in Eq. (17) to calculate the transmission coefficient \mathcal{T}_p .

In Fig. 5(a) the surface modes of the two bulk SiC materials can be nicely seen. When adding germanium layers in Fig. 5(b)-(f) we add successively new coupled modes in the spectral frequency window between ω_{TO} and ω_{LO} of SiC, i.e. the reststrahlenband. These coupled modes are the coupled surface phonon polaritons of the SiC layers which couple via the Ge layers [95]. They form new bands of modes in the reststrahlen band which are the hyperbolic bands. These hyperbolic bands are the type I and type II bands. It is interesting to note that the group velocity in the direction parallel to the interface of the modes in the type I band can be negative. This leads to negative or anomalous refraction [1, 2] which has already been measured for mHMM [22]. This negative refraction does of course also occur for near-field thermal radiation and has been studied for instance in Ref. [92] by using the energy-streamline method.

From the shown plots in Fig. 5 it is also apparent that the coupled surface mode resonances of the two bulk SiC materials which are coupled via the vacuum gap in Fig. 5 (a) persist when adding the layers of germanium. These surface modes can be formally distinguished from the hyperbolic modes: This is so because the hyperbolic modes are propagating inside the multilayer medium, i.e. they are Bloch modes, whereas the surface modes are evanescent in nature. For an infinite multilayer structure the Bloch modes are fulfilling the dispersion relation [79]

$$(\lambda = \text{s, p})$$

$$\begin{aligned} \cos(\gamma_\lambda \Lambda) = & -\frac{1}{2} \left(\frac{k_{z1}}{P_\lambda k_{z2}} + \frac{P_\lambda k_{z2}}{k_{z1}} \right) \sin(k_{z1} l_1) \sin(k_{z2} l_2) \\ & + \cos(k_{z1} l_1) \cos(k_{z2} l_2). \end{aligned} \quad (18)$$

Here, $k_{z1}^2 = \epsilon_1 \omega^2 / c^2 - \kappa^2$, $k_{z2}^2 = k_{z0}^2$, and $P_s = 1$ and $P_p = \epsilon_1$ depending on the polarization state; l_1 and l_2 are the thicknesses of the two layers and γ_λ is the Bloch wave-vector component parallel to the optical axis. In the long-wavelength limit this dispersion relation reproduces the EMT expressions in Eqs. (2) and (3).

When determining the Bloch bands from Eq. (18) and adding this information to the plots of the transmission coefficients we find the result shown in Fig. 6(a). From this figure it can be seen that the surface modes lie outside the two hyperbolic Bloch bands in the region labeled as 'SM'. For comparison we show the EMT result in Fig. 6(d). Here, we model the mHMM as a $9 \cdot \Lambda = 180$ nm layer of an effective uniaxial material with permittivities described by Eqs. (4) and (5) with $f = 0.5$ on a SiC substrate. Obviously this result is different from the exact results, since the surface modes in the 'SM' region are not included in the EMT. A fact which has important consequences for LDOS and heat flux calculations based on EMT [30, 82]. Furthermore, the hyperbolic bands predicted by EMT are extended to infinite values of κ , whereas the exact results predict Bloch bands which are limited with respect to the value of κ , i.e. for each frequency there is a maximum κ for which one can find hyperbolic Bloch modes. Finally, it is clear that the EMT makes no difference between the different kinds of configurations. In Fig. 6(a) we have chosen SiC as topmost layer for both media. We can of course also chose to make the calculations for our mHMM with Ge as topmost layers for both mHMM. Then we obtain the result shown in Fig. 6(b). The surface mode in the 'SM' region corresponding to the surface phonon polaritons of the two topmost SiC layers in Fig. 6(a) is fully suppressed in this case, so that for this configuration mainly the hyperbolic modes are contributing to the radiative heat flux for $d = 10$ nm. If we chose a mixed configuration, which means that for one mHMM SiC is the topmost layer and for the other one Ge is the topmost layer, we find the result shown in Fig. 6(c). In this case the transmission coefficient has still some traces of the surface mode contribution in the 'SM' region.

B. Radiative Heat Flux

In order to discuss the radiative heat flux, we can make use of the expressions derived in Sec. III. For small temperature differences between the two considered media, i.e. we have $T_1 = T + \Delta T$ and $T_2 = T$ with $\Delta T \ll T$, it is more convenient to study the heat transfer coefficient (HTC) instead of the heat flux Φ . The HTC is defined

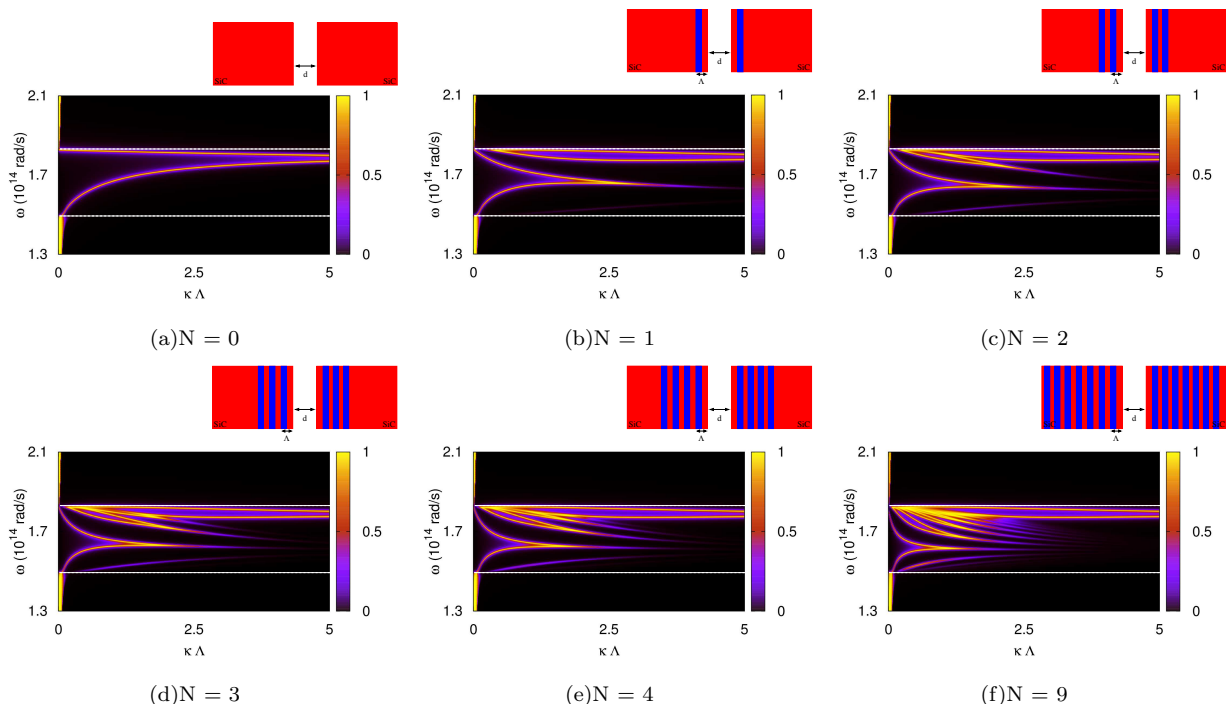


Figure 5: Transmission coefficient \mathcal{T}_p of the p-polarized modes in Eq. (17) in (ω, κ) space fixing $d = 10$ nm. The horizontal lines represent ω_{TO} and ω_{LO} of SiC, i.e. in between both lines lies the reststrahlenband. (a) two SiC bulk media. (b) first unit cell of the mHMM is achieved by adding a 10 nm thick germanium layer 10 nm below the SiC surface. This Ge/SiC layer of thickness $\Lambda = 20$ nm is the first unit-cell of an infinite Ge/SiC hMM with period Λ and filling fraction $f = 0.5$. (c)-(f) further germanium layers of 10 nm thickness are added until we have a mHMM of 9 SiC/Ge unit cells or 18 layers with an overall thickness of 180 nm. Here N stands for the number of SiC/Ge unit cells.

as

$$h = \int_0^\infty d\omega \frac{d\Theta(\omega, T)}{2\pi dT} H_\omega \quad (19)$$

where the reduced spectral heat transfer coefficient (sHTC) is

$$H_\omega = \sum_{\lambda=s,p} \int \frac{d^2\kappa}{(2\pi)^2} \mathcal{T}_\lambda(\omega, \boldsymbol{\kappa}; d) \quad (20)$$

With this definition the heat flux is itself given by $\Phi = h\Delta T$. Throughout the manuscript we set $T = 300$ K.

In Fig. 7 we first show the sHTC normalized to that of a blackbody for two SiC semi-infinite materials, two SiC/Ge mHMM with SiC as topmost layer, two SiC/Ge mHMM with Ge as topmost layer and finally the mixed case where one mHMM has SiC as topmost layer and the other one Ge as topmost layer. For comparison we have also included the results of EMT. In Fig. 7(a) we have $d = 100$ nm and therefore $d \gg \Lambda$, since $\Lambda = 20$ nm. In this case, one could expect that EMT is a very good approximation. Indeed, the EMT results are for most frequencies quite well reproducing the results of the case where SiC is the topmost layer. Nonetheless, the other two cases where Ge is the topmost layer or the mixed configuration are not well described by EMT at all which

is due to the fact that we have used SiC as substrate for the EMT calculation. But when Ge is on top then in the exact calculation we also have Ge as substrate. Therefore one needs to use a Ge substrate in the EMT calculation as well. We have checked that EMT gives a good approximation of the case where Ge is on top when using Ge as a substrate. Furthermore, it can already be seen that for two bulk SiC media the radiative heat flux is mostly narrowband and concentrated around the surface-phonon polariton resonance at $\omega_{\text{SPHP}} = 1.787 \times 10^{14}$ rad/s whereas for the mHMM also hyperbolic modes contribute inside the reststrahlenband, so that for mHMM the heat flux is broadband as discussed in Refs. [28, 29].

For extremely small distances of $d = 10$ nm, we have $d < \Lambda$. In this case it cannot be expected that EMT gives any reasonable result. By comparing EMT to the exact results in Fig. 7(b) it can be seen that the EMT results are actually not so far off from the exact results for most frequencies when SiC is topmost layer, but they lack of course the surface mode contribution of the first SiC layer as could already be observed in the transmission coefficients. This finding has important consequences for the LDOS and heat flux as discussed in Refs. [30, 31, 82]. Compared to the mixed configuration and the configuration with Ge as topmost layer EMT overestimated the heat flux inside the reststrahlenband for most frequencies, whereas compared to the configuration with SiC as

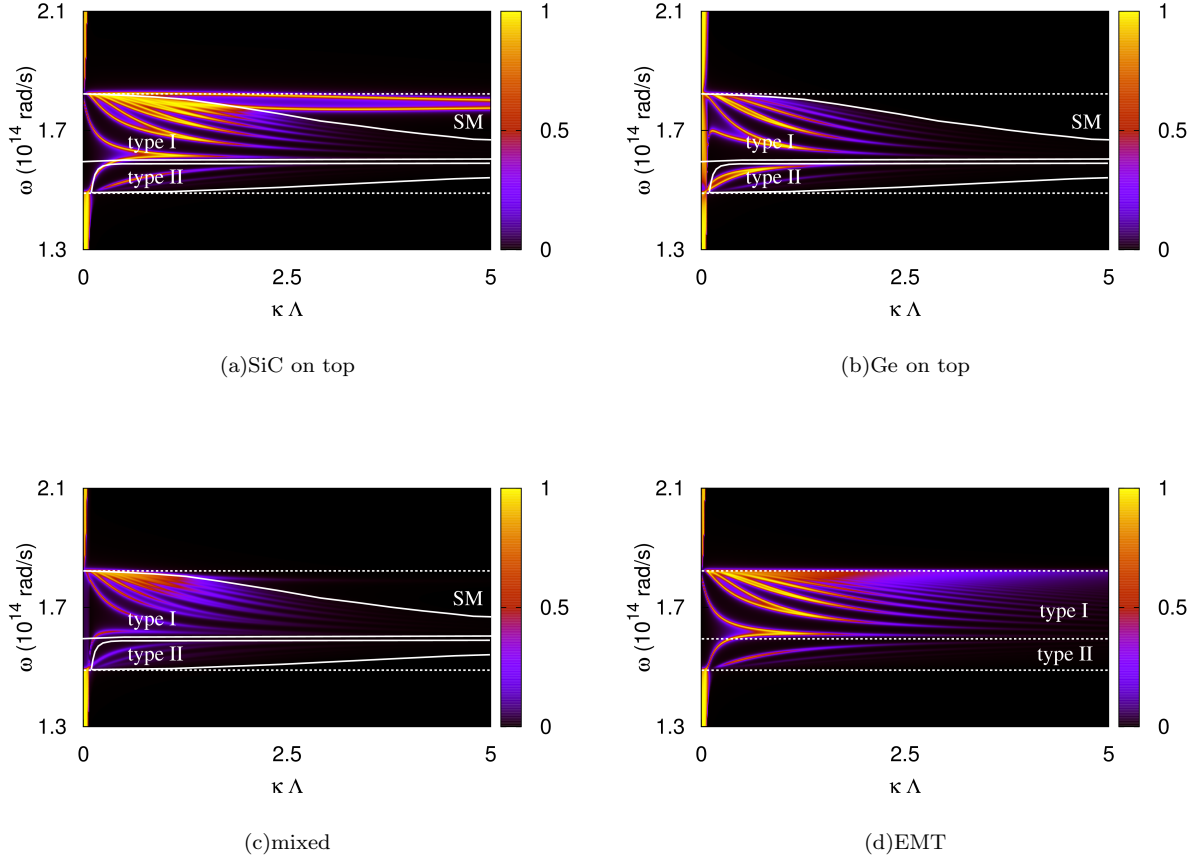


Figure 6: Transmission coefficient \mathcal{T}_p as in Fig. 5 but for different configurations. The solid white lines mark the edges of the hyperbolic bands determined with the exact dispersion relation (18) for an infinite hyperbolic structure. Here the exact results are for a structure with $N = 9$ SiC/Ge unit cells, i.e. 18 layers, so that the hyperbolic bands are not completely filled but the different modes can be seen.

topmost layer EMT underestimates the heat flux especially around ω_{SPhP} .

In Fig. 8 we show finally the HTC normalized to the blackbody value which is $h_{\text{BB}} = 6.12 \text{ W}/(\text{m}^2\text{K})$. As can be expected from the sHTC the heat flux for the mHMM with SiC as topmost layer is slightly larger than that of two SiC-SiC bulks for very small distances due to the extra contribution of the hyperbolic modes. The other configurations lead to much smaller heat fluxes for $d < 100 \text{ nm}$. The EMT result underestimates the flux for the mHMM with SiC as topmost layer and it overestimates the heat flux of the other mHMM configurations in this distance regime. Nonetheless, the EMT result coincides with the exact values when SiC is on top for distances larger than $200 \text{ nm} = 10 \cdot \Lambda$. Interestingly, in the intermediate distance regime between 100 nm and 1000 nm the mHMM with Ge as topmost layer gives larger heat fluxes than predicted by the EMT. Obviously, the overall heat flux level of mHMM is for most distances smaller than the heat flux between two simple SiC-SiC bulk materials.

C. Impact of the first single layer

Recently, the idea was brought forward that one can replace “the HMM with a single thin layer, optimized for even greater heat transfer” [96]. Therefore we want to compare the sHTC and the HTC for our SiC/Ge mHMM structure with a structure consisting of a single 10 nm layer of SiC on a semi-infinite Ge substrate. In Fig. 9 we show again the sHTC as in Fig. 7 but this time we compare the results for the different configurations of the SiC/Ge mHMM structure with the results with a structure which is simply given by a single 10 nm SiC slab on a Ge substrate. It can be seen in Fig. 7 that the sHTC for the single layer structure is quite different from the sHTC of the mHMM no matter what configuration. The two peaks which can be seen close to the edges of the reststrahlenband are due to the coupled surface phonon polaritons of the thin single layer.

When looking at the full HTC in Fig. 10 it seems that the HTC of the single layer structure is interpolating that of the mHMM with Ge as topmost layer and that with

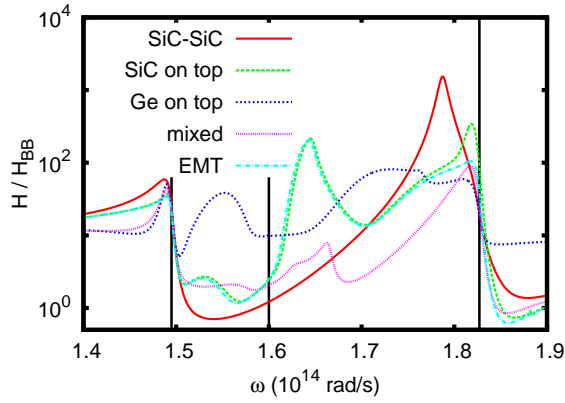
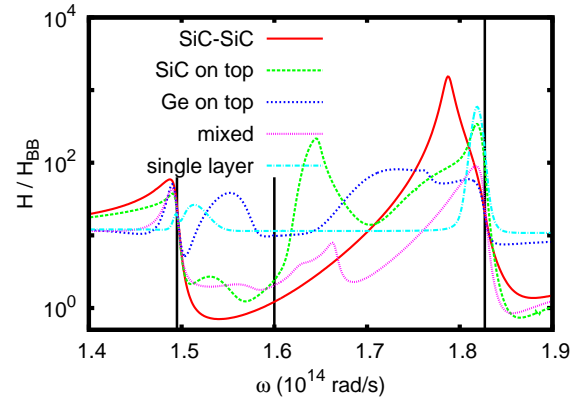
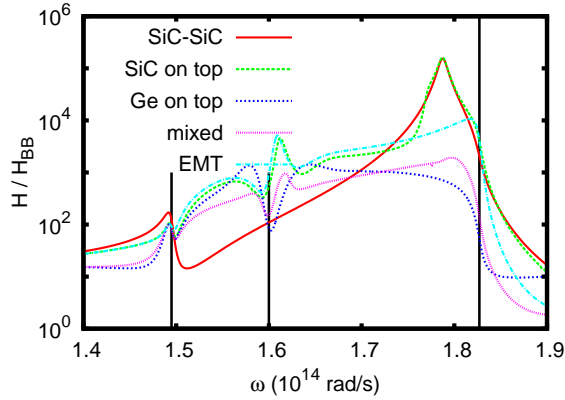
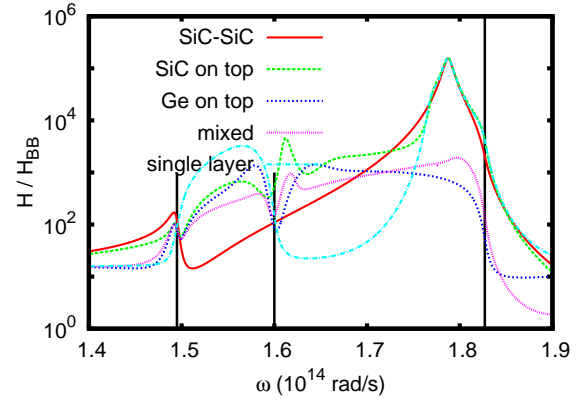
(a) $d = 100$ nm(a) $d = 100$ nm(b) $d = 10$ nm(b) $d = 10$ nm

Figure 7: Plot of the sHTC normalized to the blackbody result for different configurations and different vacuum gaps. For comparison the results of EMT are added. The vertical lines mark the edges of the hyperbolic bands.

Figure 9: Plot of the sHTC as in Fig. 7, but instead of the EMT result we plot the values of the sHTC of two structures with a single 10nm SiC layer on a Ge substrate.

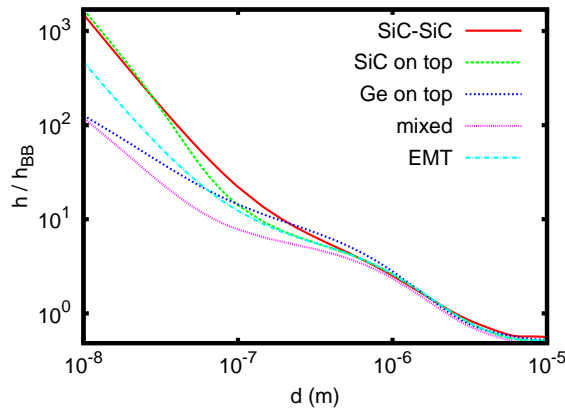


Figure 8: HTC normalized to the blackbody value $h_{BB} = 6.12 \text{ W}/(\text{m}^2\text{K})$ for two SiC half spaces, and two Ge/SiC mHMM with SiC as topmost layer, Ge as topmost layer and for the mixed case. In addition the result predicted by the EMT is plotted.

SiC as topmost layer. For $d < 100$ nm the HTC of the single layer resembles that of the mHMM with SiC on top and for $d > 100$ nm it resembles the case of the mHMM with Ge on top. Therefore the statement of Ref. [96] seems to be correct although in our plots the mHMM gives slightly larger results than the single layer structure for $d \ll 100$ nm.

To test the statement for mHMM with different Λ we have plotted in Fig. 11(a) the HTC of SiC/Ge mHMM with SiC as topmost layer with different layer thicknesses but with a fixed number of unit cells ($N = 9$) and with fixed $f = 0.5$ normalized to that of a single thin layer of SiC with the same thickness as in the mHMM on a semi-infinite Ge substrate. It can be seen that for $d < 100$ nm the HTC for the two mHMM tends to be larger than that of the single SiC films in general. Only for relatively thick layers of 50 nm and 100 nm the HTC of the mHMM is the same as that of the single layer for $d < 100$ nm. This suggests that the above statement is not precisely correct, but nevertheless one can say that when it is necessary to have large heat flux levels then mHMM seem to have no big advantage over a single film of phonon-polaritonic

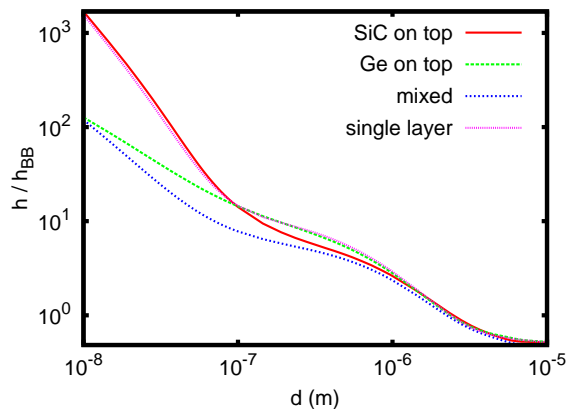


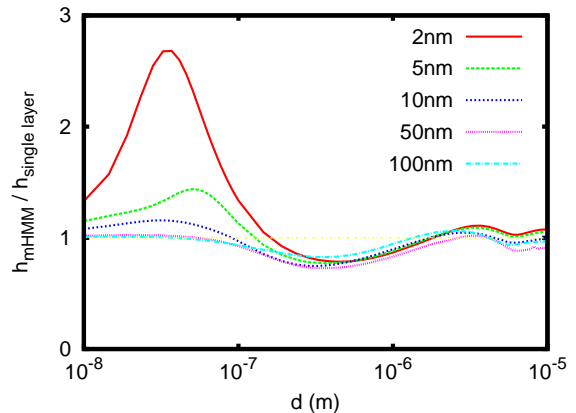
Figure 10: HTC normalized to the blackbody value $h_{\text{BB}} = 6.12 \text{ W}/(\text{m}^2\text{K})$ a SiC/Ge mHMM as in Fig. 8 but with the HTC of two structures with a single 10nm SiC layer on a Ge substrate.

material. But the same is true if one compares the HTC of the mHMM with that of bulk SiC as can be seen in Fig. 11(b). Nonetheless, with mHMM one can have larger heat fluxes than for the phonon-polaritonic bulk material or a single film of that material in particular when the period of the multilayer structure is small. We have checked that this statement remains true when Ge is the topmost layer.

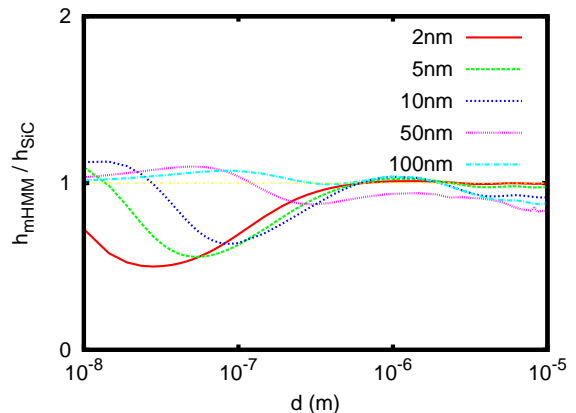
D. Surface modes vs. hyperbolic modes

One advantage of mHMM is that by choosing different orderings and filling fractions of the layers of the mHMM the frequency bands in which the material has a strong thermal emission can be controlled. Another more striking advantage is that the hyperbolic modes are propagating inside the mHMM [59, 60], whereas the surface modes are strongly confined to surface of the thermal emitter [97, 98] as is also demonstrated in Fig. 12. This property might be interesting for applications which involve the transport of heat radiation by a mHMM [61] or applications which are based on light absorption within a thick layer close to the surface like near-field thermophotovoltaics [99–102], for instance. Therefore it is reasonable to quantify the contribution of the hyperbolic modes and/or Bloch modes to the heat flux. We can separate these contributions by using Eq. (18) in order to distinguish between the Bloch modes and the surface modes of the mHMM structure.

In Fig. 13(a) we show the different contributions. For distances larger than $d = 100 \text{ nm}$ the Bloch modes which are in this case mainly the 'normal' frustrated total internal reflection modes dominate the radiative heat flux. Around $d = 100 \text{ nm}$ the hyperbolic frustrated total internal reflection modes give the largest contributions of slightly more than 50% of the total heat flux as can be seen in Fig. 13(b). For distances smaller than $d = 100 \text{ nm}$



(a)mHMM vs. single layer



(b)mHMM vs. bulk SiC

Figure 11: HTC of a SiC/Ge mHMM with SiC as topmost layer with layer thicknesses of 2 nm, 5 nm, 10 nm, 50 nm, and 100 nm ($f = 0.5$ and the number of unit cells is $N = 9$) compared to the HTC of (a) a single SiC film of same thickness as the topmost SiC layer on a Ge substrate and (b) a SiC halfspace.

the surface modes start to dominate the radiative heat flux. At $d = 10 \text{ nm}$ nearly 85% of the heat flux is due to the surface modes and nearly 15% due to the hyperbolic modes. Note, that at $d = 10 \text{ nm}$ the contribution of the hyperbolic modes is nonetheless 245 times larger than the blackbody value. If we choose Ge as topmost layer then we have already seen that the surface mode contribution is suppressed. Consequently, we can see in Fig. 13(c) and (d) that the heat flux is at $d = 10 \text{ nm}$ nearly 90% purely hyperbolic and the surface mode contribution is less than 4%. The absolute heat flux carried by the hyperbolic modes is still 114 times larger than that of a blackbody. These values can be improved by chosen smaller periods of the mHMM. A similar result is obtained in the mixed case and therefore not shown here. Hence, if a mHMM is needed which allows for a large contribution of HM to the heat flux that means if a true hyperbolic thermal emitter is needed then the configuration with Ge on top (with the material which does

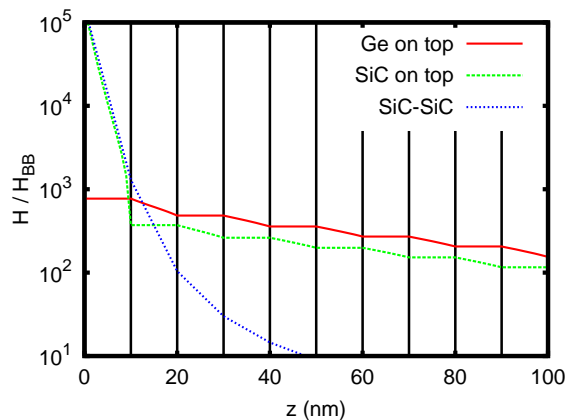


Figure 12: sHTC inside a receiver which is separated by a 10nm gap from a bulk SiC emitter at the surface phonon polariton resonance $\omega = \omega_{\text{SPHP}} = 1.787 \times 10^{14}$ rad/s. The receivers are Bulk SiC and a SiC/Ge mHMM with $\Lambda = 10$ nm and $f = 0.5$ for the case where SiC is topmost layer and Ge is topmost layer ($N = 9$). $z = 0$ is the interface of the receiver with the vacuum gap. The vertical lines mark the interfaces between the Ge and SiC layer inside the mHMM. It can be seen that the penetration depth inside the mHMM with Ge on top is much larger than in the two other cases where most of the incoming heat flux is dissipated inside the first layer or inside a region of about 10nm thickness.

not itself support surface modes) is advantageous. The absolute heat flux values cannot be as high as for bulk SiC or as for a thin SiC layer for such a true hyperbolic emitter, but the advantage is clearly that the hyperbolic modes are propagating in nature. Therefore the absorption and generation of heat is not limited to a thin layer at the surface of the emitter, but to a much broader region [59, 60].

V. SUMMARY AND CONCLUSION

In conclusion, we have reviewed in large detail the properties of mHMM. In particular we have discussed the formation of hyperbolic bands, the impact of the different configurations on the heat flux, the relative contribution of the hyperbolic heat flux channels to the full heat flux, and we have compared the heat flux for mHMM with that of a single layer structure. We have seen that the mHMM emitters are broadband in general and the full heat flux

level is in most cases only slightly larger than that of a bulk medium or a single layer. For a true mHMM emitter where the heat flux is dominated by hyperbolic modes (i.e. when Ge is topmost layer) the absolute heat flux level is typically inferior to bulk but not necessarily to single layer structures. Nonetheless, for mHMM with $\Lambda = 20$ nm it can still easily be larger than 100 times the blackbody value and for $\Lambda = 4$ nm it can be larger than 300 times the blackbody value for $d = 10$ nm. Hence, the advantage of mHMM is not necessarily the large heat flux level, but the fact that relatively large heat flux levels are combined with a large penetration depth of the heat flux, which is for mHMM by orders of magnitude larger than that of phonon-polaritonic materials as SiC [59, 60]. As a consequence the heat flux is not absorbed in an ultra-thin layer close to the surface [97] but on a relatively thick layer. This property might be exploited in thermal management applications, or for guiding near-field heat fluxes over far-field distances [61] and also for near-field thermophotovoltaics where the conversion efficiency highly depends on the volume in which the light is absorbed [101, 102].

Other realizations of hyperbolic structures made with nanowires seem to have larger heat flux levels than mHMM and might even overcome the heat flux levels of the corresponding bulk materials from which the HM are made of by purely hyperbolic heat flux channels as shown in Refs. [28, 94, 104, 105]. It has been shown recently that this performance can even be improved drastically by covering HMM with graphene [106] so that even the theoretical limit derived in Refs. [28, 107] is reached. Most of these works on nanowire HMM are based on EMT, because a full numerical treatment is not as simple as for mHMM. However, a comparison of EMT with exact results for wHMM can be found in Ref. [108] but more exact calculations are necessary to check the validity of the EMT in near-field regime.

Up-to date only a few proposals of direct applications of HMs have been suggested. Apart from the waveguide for a long range transport of the near-field heat radiation [61], HMs could open a new avenue in the near-field energy conversion to conceive broadband emitters or receivers (PV cell). Here, further studies are needed which also take into account the impact of temperature gradients inside the materials [109]. Also, the singular properties of HMs could be exploited in far-field regime to design directional thermal emitters [110], for instance.

[1] L. Hu and S. T. Chui, Phys. Rev. B **66**, 085108 (2002).
[2] D. R. Smith and D. Schurig, Phys. Rev. Lett. **90**, 077405 (2003).
[3] I. I. Smolyaninov and E. E. Narimanov, Phys. Rev. Lett. **105**, 067402 (2010).
[4] Z. Jacob, I. Smolyaninov, and E. Narimanov, Appl. Phys. Lett. **100**, 181105 (2012).

[5] A. N. Poddubny, P. A. Belov, and Y. S. Kivshar, Phys. Rev. A **84**, 023807 (2011).
[6] A. S. Potemkin, A. N. Poddubny, P. A. Belov, and Y. S. Kivshar, Phys. Rev. A **86**, 023848 (2012).
[7] J. Kim V. P. Drachev, Z. Jacob, G. V. Naik, A. Boltasseva, E. E. Narimanov, and V. M. Shalaev, Opt. Exp. **20**, 8100 (2012).

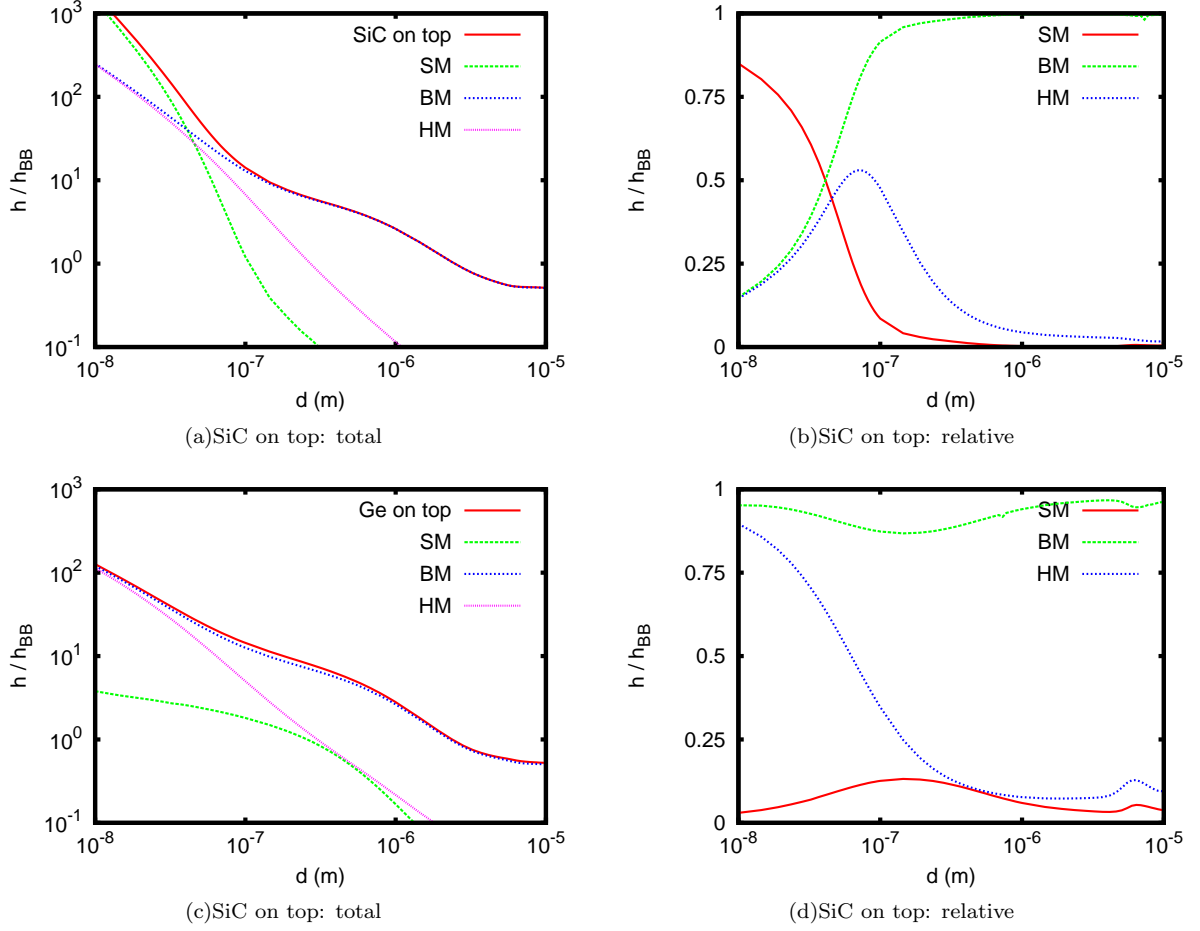


Figure 13: Here we show (a),(c) the HTC due to the surface modes (SM), Bloch modes (BM), and hyperbolic modes (HM) in comparison to the full HTC for the SiC/Ge mHMM for the two different configurations (SiC on top and Ge on top). In (b),(d) we show the relative contributions of the SM, BM and HM.

- [8] H. N. S. Krishnamoorthy, Z. Jacob, E. E. Narimanov, I. Kretzschmar, and V. M. Menon, *Science* **336**, 205 (2012).
- [9] T. Galfsky, H. N. S. Krishnamoorthy, W. Newman, E. E. Narimanov, Z. Jacob, and V. M. Menon, *Optica* **2**, 62 (2015).
- [10] Y. Wang, H. Sugimoto, S. Inampudi, A. Capretti, M. Fuji, and L. Dal Negro, *Appl. Phys. Lett.* **106**, 241105 (2015).
- [11] O. Kidwai, S. V. Zhukovsky, and J. E. Sipe, *Opt. Lett.* **36**, 2530 (2011).
- [12] A. A. Orlov, P. M. Voroshilov, P. A. Belov, and Y. S. Kivshar, *Phys. Rev. B* **84**, 045424 (2011).
- [13] A. V. Chebykin, A. A. Orlov, and P. A. Belov, *Opt. Spectr.* **109**, 938 (2010).
- [14] O. Kidwai, S. V. Zhukovsky, and J. E. Sipe, *Phys. Rev. A* **85**, 053842 (2012).
- [15] I. Iorsh, A. N. Poddubny, A. A. Orlov, P. A. Belov, and Y. S. Kivshar, *Phys. Lett. A* **376**, 185 (2012).
- [16] Z. Jacob, L. V. Alekseyev, E. Narimanov, *Opt. Exp.* **14**, 8247 (2006).
- [17] S. Feng and J. M. Elson, *Opt. Exp.* **14**, 216 (2006).
- [18] D. de Ceglia, M. A. Vincenti, S. Campione, F. Capolino, J. W. Haus, and M. Scalora, *Phys. Rev. B* **89**, 075123 (2014).
- [19] J. Bénédicto, E. Centeno, and A. Moreau, *Opt. Lett.* **37**, 4786 (2012).
- [20] E. Centeno and A. Moreau, *Phys. Rev. B* **92**, 045404 (2015).
- [21] D. R. Smith, P. Kolinko, and D. Schurig, *J. Opt. Soc. Am. B* **21**, 1032 (2004).
- [22] A. J. Hoffman, L. Alekseyev, S. S. Howard, K. J. Franz, D. Wasserman, V. A. Podolskiy, E. E. Narimanov, S. L. Sivco, and C. Gmachl, *Nature Mat.* **6**, 946 (2007).
- [23] C. Guclu, S. Campione, and F. Capolino, *Phys. Rev. B* **86**, 205130 (2012).
- [24] C. L. Cortes and Z. Jacob, *Frontiers in Optics 2013/Laser Science XXIX* (2013).
- [25] W. Newman, C. Cortes, D. Purschke, A. Afshar, Z. Chen, G. De los Reyes, F. Hegmann, K. Cadien, R. Fedosejevs, and Z. Jacob, *CLEO 2015* (2015).
- [26] S.-A. Biehs, V. M. Menon, G. S. Agarwal, *Phys. Rev B* **93**, 245439 (2016).
- [27] P. Ginzburg, A. V. Krasavin, A. N. Poddubny, P. A. Belov, Y. S. Kivshar, and A. V. Zayats, *Phys. Rev. Lett.* **111**, 036804 (2013).
- [28] S.-A. Biehs, M. Tschikin, P. Ben-Abdallah, *Phys. Rev. Lett.* **109**, 104301 (2012).

- [29] Y. Guo, C. L. Cortes, S. Molesky, and Z. Jacob, *Appl. Phys. Lett.* **101**, 131106 (2012).
- [30] S.-A. Biehs, M. Tschikin, R. Messina, and P. Ben-Abdallah, *Appl. Phys. Lett.* **102** 131106 (2013).
- [31] X. L. Liu, T. J. Bright and Z. M. Zhang, *J. Heat Transfer* **136**, 092703 (2014).
- [32] Y. Guo, Z. Jacob, *Opt. Expr.* **21**, 15014 (2013).
- [33] J. Shi, B. Liu, P. Li, L. Y. Ng, and S. Shen, *Nano Lett.* **15**, 1217 (2015).
- [34] D. W. Thompson, M. J. DeVries, T. E. Tiwald, and J. A. Woollam, *Thin Solid Films* **313-314**, 341 (1998).
- [35] J. D. Caldwell, A. Kretinin, Y. Chen, V. Giannini, M. M. Fogler, Y. Francescato, C. T. Ellis, J. G. Tischler, C. R. Woods, A. J. Giles, M. Hong, K. Watanabe, T. Taniguchi, S. A. Maier, K. S. Novoselov, *Nature Communications* **5**, 5221 (2014).
- [36] M. Esslinger, R. Vogelgesang, N. Talebi, W. Khunsin, P. Gehring, S. de Zuani, B. Gompf, and K. Kern, *ACS Photonics*, **1**, 1285(2014).
- [37] E. E. Narimanov and A. V. Kildishev, *Nature Photonics* **9**, 214 (2015).
- [38] K. Korzeb, M. Gajc, and D. A. Pawlak, *Opt. Expr.* **23**, 25406 (2015).
- [39] A. I. Volokitin and B. N. J. Persson, *Rev. Mod. Phys.* **79**, 1291 (2007).
- [40] K. Joulain, J.-P. Mulet, F. Marquier, R. Carminati, and J.-J. Greffet, *Surf. Sci. Rep.* **57**, 59-112 (2005).
- [41] S.-A. Biehs, P. Ben-Abdallah, and F. S. S. Rosa, Chapter 1 in *Infrared Radiation Nanoscale Radiative Heat Transfer and Its Applications*, InTech (2012).
- [42] K. Park, and Z. Zhang, *Front. Heat Mass Transfer* **4**, 013001 (2013).
- [43] B. Song, A. Fiorino, E. Meyhofer, and P. Reddy, *AIP Advances* **5**, 053503 (2015).
- [44] A. Kittel, W. Müller-Hirsch, J. Parisi, S.-A. Biehs, D. Reddig, and M. Holthaus, *Phys. Rev. Lett.* **95**, 224301 (2005).
- [45] L. Hu, A. Narayanaswamy, X. Chen, and G. Chen, *Appl. Phys. Lett.* **92**, 133106 (2008).
- [46] S. Shen, A. Narayanaswamy, and G. Chen, *Nano Lett.* **9**, 2909 (2009).
- [47] E. Rousseau, A. Siria, G. Jourdan, S. Volz, F. Comin, J. Chevrier and J.-J. Greffet, *Nature Photonics* **3**, 514 (2009).
- [48] R. S. Ottens, V. Quetschke, S. Wise, A. A. Alemi, R. Lundock, G. Mueller, D. H. Reitze, D. B. Tanner, and B. F. Whiting, *Phys. Rev. Lett.* **107**, 014301 (2011).
- [49] T. Kralik, P. Hanzelka, M. Zobac, V. Musilova, T. Fort, and M. Horak, *Phys. Rev. Lett.* **109**, 224302 (2012).
- [50] S. Shen, A. Mavrokefalos, P. Sambegoro, and G. Chen, *App. Phys. Lett.* **100**, 233114 (2012).
- [51] R. St-Gelais, B. Guha, L. Zhu, S. Fan, and M. Lipson, *Nano Lett.* **14**, 6971 (2014).
- [52] B. Song, Y. Ganjeh, S. Sadat, D. Thompson, A. Fiorino, V. Fernández-Hurtado, J. Feist, F. J. Garcia-Vidal, J. C. Cuevas, P. Reddy, and E. Meyhofer, *Nature Nanotechnology* **10**, 253 (2015).
- [53] K. Kim, B. Song, V. Fernández-Hurtado, W. Lee, W. Jeong, L. Cui, D. Thompson, J. Feist, M. T. Homer Reid, F. J. García-Vidal, J. C. Cuevas, E. Meyhofer, and P. Reddy, *Nature* **528**, 387 (2015).
- [54] M. Lim, S. S. Lee, and B. J. Lee, *Phys. Rev. B* **91**, 195136 (2015).
- [55] R. St-Gelais, L. Zhu, S. Fan, and M. Lipson, *Nanotechnology*, **11**, 15 (2016).
- [56] K. Kloppstech, N. Köhne, S.-A. Biehs, A. W. Rodriguez, L. Worbes, D. Hellmann, A. Kittel, arXiv:1510.06311.
- [57] I. S. Nefedov and C. R. Simovski, *Phys. Rev. B* **84**, 195459 (2011).
- [58] C. Simovski, S. Maslovski, I. Nefedov, and S. Tretyakov, *Optics Express* **21**, 14988 (2013).
- [59] S. Lang, M. Tschikin, S.-A. Biehs, A. Y. Petrov, and M. Eich, *Appl. Phys. Lett.* **104**, 121903 (2014).
- [60] M. Tschikin, S.-A. Biehs, P. Ben-Abdallah, S. Lang, A. Y. Petrov, and M. Eich, *JQSRT* **158**, 17 (2015).
- [61] R. Messina, P. Ben-Abdallah, B. Guizal, M. Antezza, S.-A. Biehs, *Phys. Rev. B* **94**, 104301 (2016).
- [62] J. Liu and E. E. Narimanov, *Phys. Rev. B* **91**, 041403(R) (2015).
- [63] S.-A. Biehs, S. Lang, A. Yu. Petrov, M. Eich, and P. Ben-Abdallah, *Phys. Rev. Lett.* **115**, 174301 (2015).
- [64] Y. Guo and Z. Jacob, *J. Appl. Phys.* **115**, 234306 (2014).
- [65] E. Monca-Villa, V. Fernández-Hurtado, F. J. García-Vidal, A. García-Martín, and J. C. Cuevas, *Phys. Rev. B* **92**, 125418 (2015).
- [66] X. L. Liu and Z. M. Zhang, *Appl. Phys. Lett.* **107**, 143114 (2015).
- [67] A. I. Volokitin and B. N. J. Persson, *Phys. Rev. B* **63**, 205404 (2001).
- [68] S.-A. Biehs, *EPJ B* **58**, 423 (2007).
- [69] M. Francoeur, P. Mengüç, R. Vaillon, *Appl. Phys. Lett.* **93**, 043109 (2008).
- [70] P. Ben-Abdallah, K. Joulain, J. Drevillon, and G. Domingues, *JAP* **106**, 044306 (2009)
- [71] A. Narayanaswamy and G. Chen, *J. Quant. Spect. Rad. Transf.* **93**, 175 (2005).
- [72] M. Tschikin, P. Ben-Abdallah, and S.-A. Biehs, *Phys. Lett. A* **376**, 3462 (2012).
- [73] W. T. Lau, J.-T. Shen, G. Veronis, S. Fan, and P. V. Braun, *Appl. Phys. Lett.* **92**, 103106 (2008).
- [74] W. T. Lau, J.-T. Shen, S. Fan, *Phys. Rev. B* **80**, 155135 (2009).
- [75] P. Ben-Abdallah, K. Joulain and A. Pryamikov, *Appl. Phys. Lett.* **96**, 143117 (2010).
- [76] A. Pryamikov, K. Joulain, P. Ben-Abdallah, J. Drevillon, *J. Quant. Spect. Rad. Transf.* **112**, 1314 (2011).
- [77] M. Francoeur, P. Mengüç, and R. Vaillon, *J. Quant. Spect. Rad. Transf.* **110**, 2002 (2009).
- [78] S. I. Maslovski, C. R. Simovski, S. A. Tretyakov, *Phys. Rev. B* **87**, 155124 (2013).
- [79] P. Yeh, *Optical Waves in Layered Media*, (Wiley, Hoboken, 2005).
- [80] W. Yan, M. Wubs, and N. A. Mortensen, *Phys. Rev. B* **86**, 205429 (2012).
- [81] V. P. Drachev, V. A. Podolskiy, and A. V. Kildishev, *Opt. Expr.* **21**, 15048 (2013).
- [82] M. Tschikin, S.-A. Biehs, R. Messina, P. Ben-Abdallah, *J. Opt.* **15**, 105101 (2013).
- [83] *Handbook of Optical Constants of Solids*, edited by E. Palik (Academic Press, New York, 1998).
- [84] C. F. Bohren and D. R. Huffman, *Absorption and Scattering of Light by Small Particles* (Wiley, New York, 1998).
- [85] S. Lang, H. S. Lee, A. Yu. Petrov, M. Störmer, M. Ritter, and M. Eich, *Appl. Phys. Lett.* **103**, 021905 (2013).
- [86] D. Polder and M. van Hove, *Phys. Rev. B* **4**, 3303 (1971).
- [87] S.A. Biehs, P. Ben-Abdallah, F. S. S. Rosa, K. Joulain,

- J. J. Greffet, *Optics Express*, **19**, A1088-A1103 (2011).
- [88] G. Bimonte and E. Santamato, *Phys. Rev. A* **76**, 013810 (2007).
- [89] R. Messina and M. Antezza, *Phys. Rev. A* **84**, 042102 (2011).
- [90] M. Krüger, G. Bimonte, T. Emig, and M. Kardar, *Phys. Rev. B* **86**, 115423 (2012).
- [91] S.-A. Biehs and P. Ben-Abdallah, *Phys. Rev. B* **93**, 165405 (2016).
- [92] T. J. Bright and X. L. Liu and Z. M. Zhang, *Opt. Expr.* **22**, A1112 (2014).
- [93] H. Wu, Y. Huang, and K. Zhu, *Optics Letters* **40**, 4532 (2015).
- [94] J.-Y. Chang, S. Basu, Y. Yang, and L. Wang, *J. Appl. Phys.* **119**, 213108 (2016).
- [95] S. V. Zhukovsky, A. Andryieuski, J. E. Sipe, and A. V. Lavrinenko, *Phys. Rev. B* **90**, 155429 (2014).
- [96] O. D. Miller, S. G. Johnson, and A. W. Rodriguez, *Phys. Rev. Lett.* **112**, 157402 (2014).
- [97] S. Basu and Z. M. Zhang, *Appl. Phys. Lett.* **95**, 133104 (2009).
- [98] S. Basu and M. Francoeur, *Appl. Phys. Lett.* **99**, 143107 (2011).
- [99] R. S. DiMatteo, P. Greiff, S. L. Finberg, K. A. Young-Waithe, H. K. Choy, M. M. Masaki, and C. G. Fonstad, *Appl. Phys. Lett.* **79**, 1894 (2001).
- [100] A. Narayanaswamy and G. Chen, *Appl. Phys. Lett.* **82**, 3544 (2003).
- [101] K. Park, S. Basu, W. P. King, and Z. M. Zhang, *J. Quant. Spect. Rad. Transf.* **109**, 305 (2008).
- [102] M. P. Bernardi, O. Dupré, E. Blandre, P.-O. Chapuis, R. Vaillon and M. Francoeur, *Scientific Rep.* **5**, 11626 (2015).
- [103] M. Auslender and S. Have, *Opt. Lett.* **21**, 1765 (1996).
- [104] B. Liu and S. Shen, *Phys. Rev. B* **87**, 115403 (2013).
- [105] X.L. Liu, R.Z. Zhang, Z.M. Zhang, *Int. J. Heat Mass Transfer* **73**, 389 (2014).
- [106] X. Liu, R. Z. Zhang, and Z. Zhang, *ACS Photonics* **1**, 785(2014).
- [107] O. D. Miller, S. G. Johnson, and A. W. Rodriguez, *Phys. Rev. Lett.* **115**, 204302 (2015).
- [108] M. S. Mirmoosa, F. Rütting, I. S. Nefedov, and C. R. Simovski, *J. Appl. Phys.* **115**, 234905 (2014).
- [109] R. Messina, W. Jin, A. W. Rodriguez, *Phys. Rev. B* **94**, 121410(R) (2016).
- [110] G. Barbillon, J.-P. Hugonin, S.-A. Biehs, P. Ben-Abdallah, arXiv:1605.01247 (2016).